Journal of the Korean Physical Society (2023) 82:985–991
https://doi.org/10.1007/s40042-023-00740-x

Online ISSN 1976-8524
Print ISSN 0374-4884

ORIGINAL PAPER - CROSS-DISCIPLINARY PHYSICS AND RELATED AREAS OF SCIENCE AND TECHNOLOGY

The early development of synchrotron white-beam X-ray topography analysis for crystal investigations at Pohang light source-II

Ho Jae Kwak[1] · **Kangwoo Ahn**[1] · **Jae-Hong Lim**[1] · **Jong Hyun Kim**[1,2]

Received: 14 December 2022 / Revised: 9 January 2023 / Accepted: 9 January 2023 / Published online: 17 April 2023

Abstract

Given the limitations imposed by the physical properties of silicon semiconductors, various wide-bandgap-based semiconductor materials are being actively developed and utilized. Also, the use of crystalline materials such as diamond has been increasing in recent years. An understanding of crystal quality and the extent of internal defects is becoming increasingly important for the development and application of such crystalline materials. X-ray topography (XRT) nondestructively yields information on crystal surfaces and internal defects. In particular, XRT using synchrotron X-rays quickly provides high-resolution images of defects in single crystals. Here, we confirmed the utility of synchrotron white-beam XRT (SWXRT). We established the technique and used it to evaluate the characteristics of a representative, wide-bandgap-based semiconductor material. The SWXRT installed in the 9D beamline of the Pohang accelerator laboratory has an eight-axis sample stage and three-axis detector motion and thus defects in wafers several inches in size in various XRT measurement modes. The SWXRT device not only accepts analog X-ray film, but also yields large-area panel images and data for high-resolution X-ray cameras. We used high-resolution X-ray film and a digital detector to rapidly acquire and analyze the diffraction image of the SiC substrate, which is a representative single-crystal power semiconductor. We expect the quality and defect information of various monocrystalline materials to increase in the near future.

Keywords X-ray topography · Synchrotron · Single crystal · Diffraction imaging

1 Introduction

Single-crystal materials exhibit better electrical, optical, thermal, and mechanical properties than polycrystalline materials because of their highly ordered structures and thus find applications in various industrial fields, particularly as next-generation semiconductors for high-performance, high-speed devices. Representative single-crystal materials include SiC [1, 2] for high-power devices, GaN [3–5] for high-frequency communication devices requiring high-level electron mobility, and diamond [6–8] for instruments requiring good thermal conductivity. Recently, gallium oxide has been studied as a next-generation power semiconductor material because of its wide bandgap [9–11]. CVD-based crystalline diamond is evaluated in terms of heat dissipation for optical applications that require good thermal conductivity and optical transparency [12–14]. It is expected that such materials will be increasingly applied.

Single crystals may acquire defects during growth and substrate manufacture. To maintain high quality, it is important to identify the causes of defects, and then reduce them during both growth and manufacturing. Defects degrade the required characteristics and/or compromise reliability; therefore, several techniques have been used to address this problem. Transmission electron microscopy and X-ray diffraction evaluate internal crystallinity, and laser polarization and scanning electron microscopy detect surface defects. The main defects of SiC single crystals are micro-pipes and threading screw dislocations (TSDs) [15]. These common

---

Ho Jae Kwak and Kangwoo Ahn have contributed equally to this work.

✉ Jong Hyun Kim
kjh9818@postech.ac.kr

[1] Pohang Accelerator Laboratory, 80 Jigokro-127-Beongil, Nam-gu, Pohang, Gyeongbuk, Korea

[2] Department of Mechanical Engineering, Pohang University of Science and Technology, 77 Cheongam-Ro. Nam-Gu, Pohang, Gyeongbuk, Korea

defects severely compromise electronic characteristics. Etch pit density (EPD) can be mainly used to evaluate the extent of such defects [16, 17]. However, EPD destroys the sample surface and it is impossible to recycle the expensive materials after measurement [18].

X-ray topography (XRT) is a nondestructive X-ray diffraction technique that has been extensively studied since the mid-twentieth century. XRT quickly detects defects in single crystals [19–22]. The diffraction signals of X-rays incident on a crystal are collected as a contrast image. Defects change the contrast within image, which allows easy visualization of grain boundaries, twins, stacking defects, precipitates, and voids. XRT can handle crystals with sizes of several hundred micrometers to several tens of millimeters, such as semiconductor substrates. Moreover, sample pre-treatment is not required. XRT using synchrotron X-rays has a flux about 10,000-fold that of conventional X-ray generators and a smaller beam divergence, and thus provides a large number of high-resolution XRT images very quickly. A lot of development for X-ray techniques [23–30] are still in progress, and beamlines including XRT [31–35] have been constructed in several synchrotron accelerators, but not in the Pohang accelerator laboratory (PLS-II) until now.

Here, we describe a unique XRT system using a synchrotron white-beam of the PLS-II beamline 9D and our preliminary experimental results. The synchrotron white-beam XRT (SWXRT) allows the samples and detector to move freely, both linearly and through all azimuthal angles; it is designed to obtain signals from large single crystals. Analog X-ray films, and flat panel and X-ray detectors, can be used to quickly and easily identify topographically defective areas on large high-resolution images. We imaged several representative defects of a single-crystal SiC substrate using various detectors.

2 Experiments and discussion

XRT analyzes crystal defects by measuring the diffraction signals emitted when X-rays are incident on a crystal. Those signals follow the Bragg law; a diffraction image is generated via interference of the diffracted X-rays depending on the crystal structure. In the diffraction image of a sample that is perfectly crystalline, image brightness should be uniform along the crystal plane. However, if there is a local defect or non-uniformity in the lattice plane, the Bragg law cannot be followed, a contrast change occurs around the defect. This locates the defects, the extent and type of which can be determined by analyzing contrast patterns.

Synchrotron X-ray beams exhibit much brighter and more parallel beams than conventional X-ray sources. Thus, the data acquisition time is short and beam dispersion is minimal; spatial resolution is enhanced by increasing the distance between the light source and sample. The PLS-II X-rays exhibit a high flux of $10^4 \sim 10^8$ times and beam deviation of several mrad. Given the long distance (about 20 m) between the source and sample, excellent spatial resolution is possible, and a large-area XRT image can be obtained in one experiment using a bright beam 150 mm in width. The white-beam X-rays of the bending magnets in the 9D PLS-II beamline show wide spectral characteristics and good signal-to-noise ratios. SWXRT using this beamline yields clear images of multiple diffraction points simultaneously and it is easy to analyze crystal defects. Also, the defect structure can be investigated by in situ experiments controlling external stimuli such as the electromagnetic field, thermal gradient, and/or pressure around the sample. SWXRT is one of the most advanced nondestructive techniques available today.

A dedicated SWXRT system was installed in the PLS-II 9D beamline; an optical schematic is shown in Fig. 1 (a). The beamline has very straight high-brightness X-rays that are derived from the storage beam (3.0 GeV, 400 mA) using a bending magnet; the XRT equipment is located about 20 m from the beam source. The main spectral range of X-rays in the 9D beamline is about 4–40 keV. White-beam X-rays passing through the optical slit to become incident on a sample exhibit a brilliance of about 4×10^{12} photon/s/0.1% BW at 20 keV when the beam current is 400 mA, and the beam size can be extended 150 mm in the horizontal direction (divergence of 8 mrad) and about 6 mm at 20 keV in the vertical direction. The parameters of the 9D beamline are listed in Table 1.

The SWXRT system in the 9D beamline has a sample stage that controls the direction of the crystal and an X-ray detector arm that detects diffraction signals emitted from the sample in various directions. Figure 1 (b,c) shows the measurement scheme and an image of the SWXRT diffractometer, which is about 900 mm in both width and length and about 1,000 mm in height (and thus assumes the form of a table); the eight-axis sample stage is at the top center. The X-ray detector arm moves in two directions around the specimen stage, i.e., in the azimuthal and altitudinal (2θ) directions. In the latter direction, it is possible to increase the angle of the X-ray detector arm to vertical (90º); the detector then points downward. The altitude ranges from 0º to 180º, but if angle is too low position, the detector may be directly irradiated; caution is thus required. The X-ray detector arm can be rotated 360º in the azimuthal direction. The total length of the X-ray detector arm is 1,000 mm. The arm is equipped with a linear guide and ball-screw shaft that moves the detector longitudinally. The distance between the sample and detector can be adjusted from about 10 to 80 cm. By adjusting the distance, the entire sample can be analyzed or high-resolution signals can be obtained from specific regions. On the opposite side of the detector arm, a counterbalance is installed to facilitate angular movement in

Fig. 1 **a** Overview of the PLS-II 9D beamline used for novel SWXRT analysis, **b** schematic of X-ray topography in grazing incidence mode, **c** the SWXRT system at PLS-II

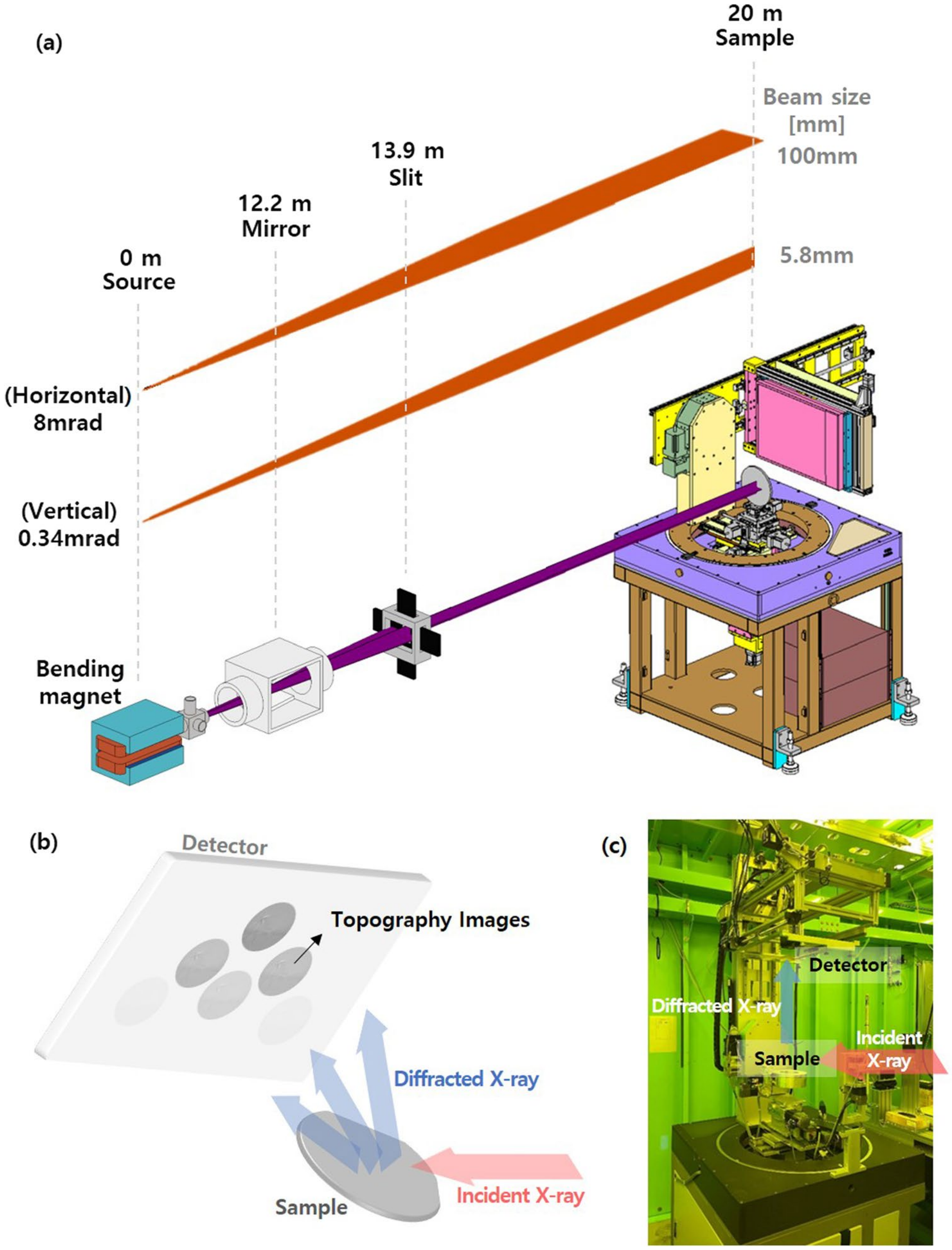

the altitudinal direction. Given the motions of the arm, grazing incidence, transmission, and back-reflection geometry, which are the main XRT measurement modes, are available.

The optical resolution of the XRT image is determined as follows:

$$R = S \times \frac{D_d}{D_s}$$

where R is the resolution, S is the size of the source, D_d is the sample-detector distance, and D_s is the sample-source distance [36]. The size (S) of the X-ray source is 60 × 30 μm (H × V) after passing through the bending magnet, and the

Table 1 Beamline parameters

Type	Bending magnet
X-ray flux	10^{12} photons/s/0.1% BW
Beam size at source	60 (H) × 30 (V) μm
Beam size at sample	Max. 150 (H) × 5.8 (V) mm
X-ray wavelength	4 ~ 40 keV
Beam divergence (horizontal)	8 mrad
Maximum sample size (in grazing incidence mode)	4 inches (dia.) or 100 × 100 mm^2

distance (D_s) from the sample position to the source is about 20 m. Therefore, the geometrical image resolution (R) of the SWXRT system in the 9D beamline is determined by the D_d between 10 and 50 cm and, as shown in Table 2, ranges from 0.31 × 0.14 µm (H × V) to 1.53 × 0.72 µm. For analog X-ray film, the highest resolution is about 1 ~ 2 µm; the SWXRT system thus allows for analysis without loss of spatial resolution.

It is important to acquire large-area high-resolution diffraction images to obtain detailed information on crystal defects inside wafer-level samples. However, current digital X-ray cameras do not match the resolution of analog X-ray films because of the pixel size and other electronic restrictions, and high-resolution X-ray cameras have a limited field of view (FOV). Analog film may be optimal but it must be developed using chemical preparations, which is inconvenient. Also, the acquired diffraction image must be re-digitized. To deal with these issues, a large-area digital flat panel X-ray detector (FXRD-1417SA; FPD) is installed on the detector arm Fig. 2a; combined with analog X-ray film (AGFA DSSC), these devices yield large-area high-resolution diffraction images [Fig. 2b]. The maximum detection area of the flat panel is 432 × 348 mm, the external dimensions are 551 × 306 × 62 mm, the weight is 7.6 kg, the effective pixel size is about 140 µm, and the scintillator is CsI. However, a detector this large may not yield high-resolution XRT images. As shown in Fig. 2c, an additional high-resolution X-ray detector (i.e., a fiber-optic-coupled sCMOS detector; ZYLA5.5X-FO; Andor) is installed on a stage that moves vertically and horizontally behind the flat panel detector and yields high-resolution digital images. As the geometrical resolution of SWXRT is superior to that of analog X-ray film, the pixel size, i.e., the resolution of the digital X-ray detector, determines the maximum resolution. The high-resolution X-ray detector has a maximum detection area of 16.6 × 14 mm and pixel size of 6.5 µm. By moving the camera horizontally and vertically, multiple XRT images can be obtained and reconstructed into large-area XRT images. The high-resolution detector is moved to a specific Laue spot location identified by the flat panel detector. The size of the beam incident on the sample is adjusted using the slit and multiple images are acquired while moving the sample. The images are then reconstructed into a large-area digital image. However, image resolution remains limited. Therefore, a darkroom for developing analog X-ray

Table 2 Theoretical image resolutions of SWXRT

Distance (cm)	Horizontal resolution (µm)	Vertical resolution (µm)
10	0.31	0.14
30	0.92	0.43
50	1.53	0.72

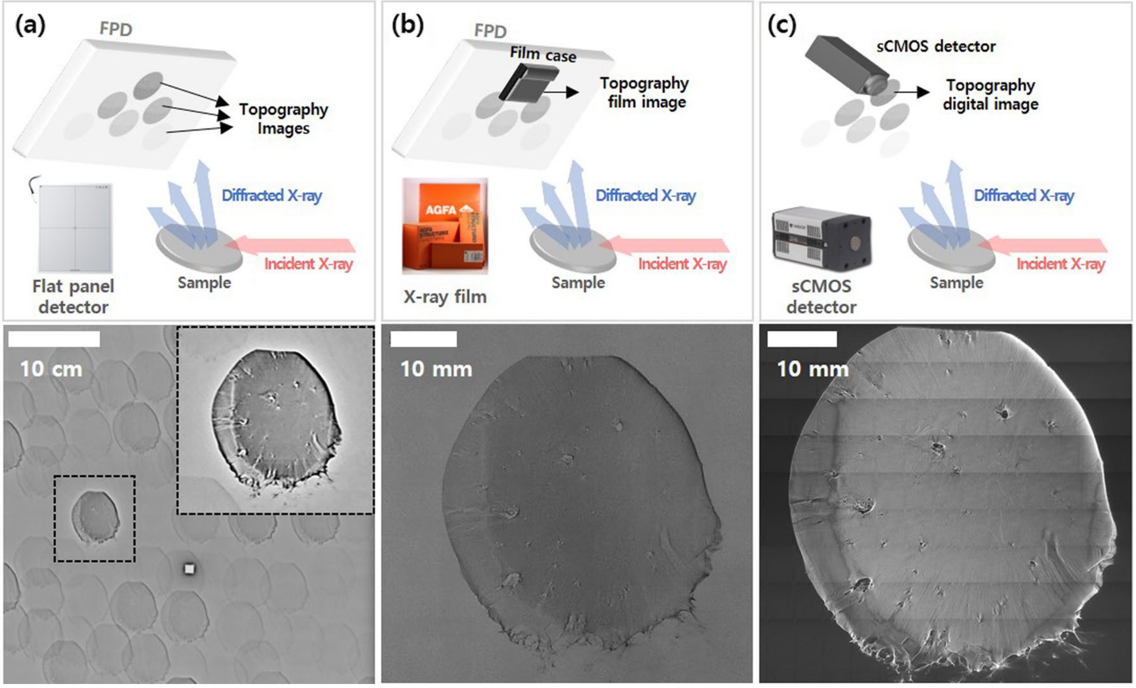

Fig. 2 Concept and setup of the SWXRT, and diffraction images obtained using a **a** flat panel detector, **b** film, and **c** fiber-optic-coupled sCMOS detector

films is available; both digital images and analog X-ray films can be used.

We prepared a silicon carbide (SiC) single-crystal substrate and obtained internal and external nondestructive diffraction images. The wafer diameter was 2 inches and no abnormality was apparent to the naked eye. Bragg mode diffraction spots were obtained based on the Berg–Barrett geometry of the 9D beamline. The X-ray detector angle was almost 90º. First, using the large-area flat panel detector, the XRT conditions (i.e., the sample position and orientation, and distance from the detector) were optimized. Then, an analog X-ray film was attached to the FPD surface and high-resolution images were obtained. The exposure time was controlled by an X-ray shutter in front of the sample. When white-beam X-rays irradiated the SiC wafer, many Bragg diffraction spots were detected on the large-area flat panel. As shown in the image on the left of Fig. 3, overlap was extensive. By controlling the position and orientation of the SiC wafer, the entire wafer surface was imaged, and the distance between the sample and detector was adjusted to detect non-overlapping diffraction spots. The resolution of the image was over 140 μm due to pixel size of detector; therefore, the internal structure was not clearly visible. Nevertheless, the XRT conditions were easily optimized. Analog X-ray films were attached to the detector at the locations of diffraction spots and then exposed and developed in the dark room to yield the high-resolution images in Figs. 4, 5. The image interiors are non-uniform, and the intensities and patterns vary because the substrate exhibits poor overall crystallinity and, in some areas, no crystallinity at all. Accordingly, it is known that the substrate growth had not been optimized and the positions and types of defects were identified by analyzing the image. There seem to be some image distortions in wafer shape, which is caused by geometry relationship of incidence beam angle and detector position. Detection of X-ray was measured a flat surface like large size X-ray film even though diffraction spot happens the surface area of Ewald sphere. However, the crystal quality and defect location could be distinguished by relative position of SiC substrate.

Regions of interest were located using the large-area flat panel detector and XRT images were acquired using

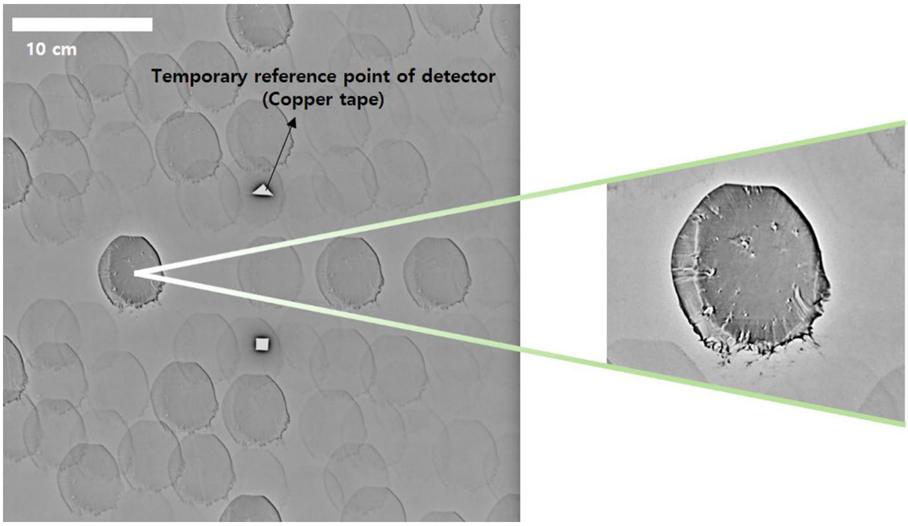

Fig. 3 White-beam XRT image of the SiC wafer. (Left) Laue spot imaging of SiC with the flat panel. (Right) magnified image of SiC

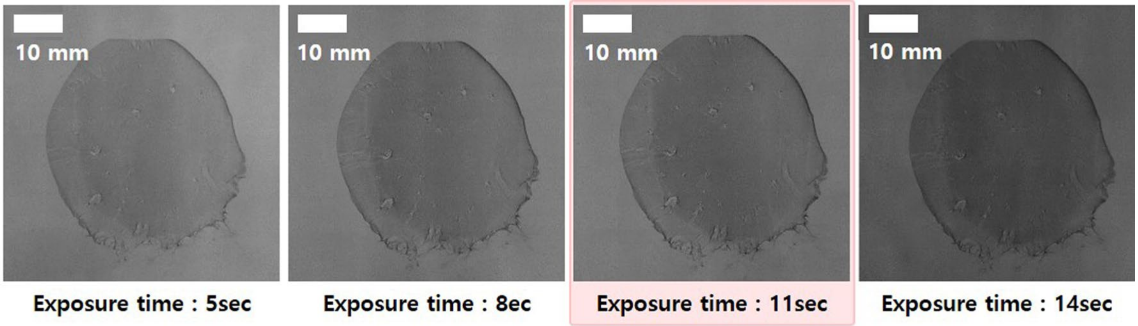

Fig. 4 Film images at various exposure times

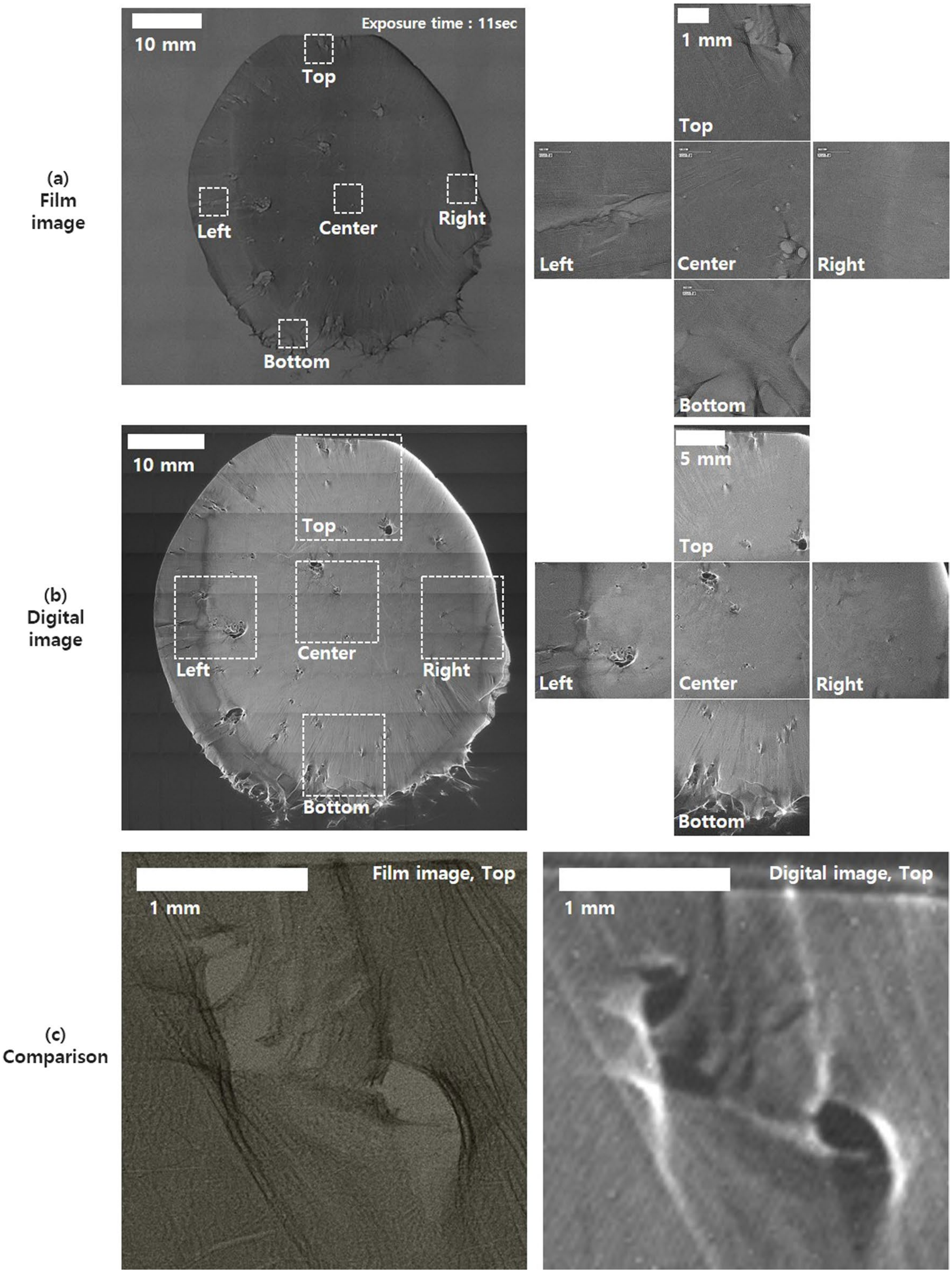

Fig. 5 The high-resolution **a** X-ray film image and **b** digital XRT image array and **c** comparison at the same position of 2” SiC wafer.(Top)

a high-resolution X-ray camera. Figure 5 shows the final image obtained by combining the high-resolution digital diffraction images of a 2-inch large-area SiC single crystal. The FOV of the high-resolution camera is 16.6× 14 mm; 108 images were acquired for the better image stitching as a 9×12 matrix by moving the sample stage horizontally and vertically. Many crystal defects are apparent at the edge, and many internal pores and several crystal defects can also be seen. Thus, the high quality XRT analysis of large size substrates can be checked and, if necessary, improved by digital X-ray topography directly.

The SWXRT system uses an azimuth-based motion stage to acquire XRT images in various directions and can therefore readily obtain and analyze large-area XRT images of several inches or more. The quality and internal defects of any single crystal can be evaluated very quickly. If necessary, typical XRT analysis, i.e., high-resolution imaging with a small FOV is also possible, followed by determination of defect density or type. This dedicated XRT analysis could be carried out very rapidly using the PLS-II synchrotron X-rays.

3 Conclusion

The PLS-II previously lacked XRT capacity. We built a SWXRT system using PLS-II white-beam X-rays, which allows for quality evaluation of single crystals at a wafer-level. The SWXRT in the 9D beamline detects diffraction spots quickly. Both the sample and detector move on several axes; various XRT modes can be used to facilitate large-area single-crystal substrate and wafer analyses. After diffraction spots are located on the large-area flat detector, high-resolution XRT images can be quickly obtained using analog X-ray film or an X-ray detector. For the demonstration of validation, the single-crystal quality of the SiC substrate was rapidly evaluated and the results were presented as large-area high-resolution images that clearly identified various internal defects. This wafer-level quality evaluation capability will help manufacturers optimize single-crystal growth control.

In the future, the novel digital based SWXRT instrumentation is going to be improved for the simple and full-automated measurement to examine near single-crystal characteristics such as GaN, Ga_2O_3 as well as SiC. Furthermore, various additional equipment will be considered to make observations of defect structure evolution under external stress such as high temperature. Moreover, the dedicated defect analysis program would be also developed for the quick confirmation of crystal quality.

Acknowledgements We thank Ms. Jin-A Kim of Pohang Accelerator Laboratory and Mr. Hyun Wook Park of WIZsystem for conducting the experiments and sharing experience in SWXRT. This work was supported by the National Research Foundation of Korea (NRF) grant funded by the Korea government (No. 2021R1C1C1010187 and No. 2021R1F1A1063106) and experiments at PLS-II 9D beamline were supported in part by MSIT and POSTECH.

References

1. J. Millan et al., IEEE Trans. Power Electron. **29**(5), 2155 (2014)
2. S. Ji, Z. Zhang, F. Wang, CES Transact Elect Mach Sys **1**(3), 254 (2017)
3. I. Akasaki, J. Cryst. Growth **195**, 248 (1998)
4. K. Okamoto et al., Jpn. J. Appl. Phys. **45**, 1197 (2006)
5. S. Nakamura, Jpn. J. Appl. Phys. **30**, 1705 (1991)
6. J. Isberg et al., Diam. Relat. Mater. **13**, 320 (2004)
7. M. Schreck et al., MRS Bull. **39**, 504 (2014)
8. M. Schreck et al., J. Appl. Phys. **127**, 125102 (2020)
9. H. Xue et al., Nanoscale Res. Lett. **13**, 290 (2018)
10. Y. Wang et al., IEEE Electron Device Lett. **41**, 131 (2020)
11. H. Sheoran, V. Kumar, R. Singh, A.C.S. Appl, Electron. Mater. **4**, 2589 (2022)
12. Z. Qi et al., Appl. Therm. Eng. **177**, 115489 (2020)
13. Y. Han et al., IEEE Transactions on Components. Pack Manufact TechnoL **4**, 983 (2014)
14. V. Ralchenko et al., Phys. Rev. Applied **16**, 014049 (2021)
15. C. Yi, D. Michael, Appl. Phys. Lett. **91**, 141918 (2007)
16. Y.-Z. Yao et al., Jpn. J. Appl. Phys. **50**, 075502 (2011)
17. D. Zhuang, J. Edgar, Mater. Sci. Eng. R. Rep. **48**, 1 (2005)
18. K. Adamczyk, G. Stokkan, M. Di Sabatino, MethodsX **5**, 1178 (2018)
19. J.-I. Chikawa, Y. Asaeda, I. Fujimoto, J. Appl. Phys. **41**, 1922 (1970)
20. B.R. David, L.G. Gabrielle, X-Ray Topograp. **11**, 332 (2004)
21. Y. Ishikawa et al., J. Electron. Mater. **47**, 5007 (2018)
22. Y. Liu et al., J. Cryst. Growth **551**, 125903 (2020)
23. Y. Kim, B.G. Cho, T.Y. Koo, J. Korean Phys. Soc. **81**, 273 (2022)
24. B.G. Cho et al., J. Korean Phys. Soc. **78**, 467 (2021)
25. J. Lee et al., J. Korean Phys. Soc. **80**, 859 (2022)
26. J. Kim et al., J. Korean Phys. Soc. **9**, 53 (2022)
27. J. Ko et al., J. Korean Phys. Soc. **77**, 363 (2020)
28. H. Jang et al., J. Korean Phys. Soc. **80**, 175 (2022)
29. Z. Jiang et al., J. Korean Phys. Soc. **79**, 697 (2021)
30. K. Park et al., J. Korean Phys. Soc. **77**, 802 (2020)
31. S. Kawado et al., J. Synchrotron Rad. **9**, 166 (2002)
32. S. Stoupin et al., AIP Conf. Proc. **1**, 1741 (2016)
33. J. Guo et al., ECS Trans. **86**, 75 (2018)
34. R. Barrett et al., J. Phys. D Appl. Phys. **28**, 250 (1995)
35. W.M. Vetter, M. Dudley, Phil. Mag. **86**, 1209 (2006)
36. A. Pogany, D. Gao, S.W. Wilkins, Rev. Sci. Instrum. **68**, 2774 (1997)